Anomalous Hall effect in the noncollinear antiferromagnetic antiperovskite $Mn_3Ni_{1-x}Cu_xN$

K. Zhao,[1,*] T. Hajiri,[2] H. Chen,[3] R. Miki,[2] H. Asano,[2] and P. Gegenwart[1]

[1]*Experimentalphysik VI, Center for Electronic Correlations and Magnetism, University of Augsburg, 86159 Augsburg, Germany*

[2]*Department of Materials Physics, Nagoya University, Nagoya 464-8603, Japan*

[3]*Department of Physics, Colorado State University, Fort Collins, Colorado 80523-1875, USA*

(Received 11 April 2019; published 9 July 2019; corrected 16 March 2020)

We report the anomalous Hall effect (AHE) in antiperovskite Mn_3NiN with substantial doping of Cu on the Ni site (i.e., $Mn_3Ni_{1-x}Cu_xN$), which stabilizes a noncollinear antiferromagnetic (AFM) order compatible with the AHE. Observed on both sintered polycrystalline pieces and single crystalline films, the AHE does not scale with the net magnetization, contrary to the conventional ferromagnetic case. The existence of the AHE is explained through symmetry analysis based on the Γ_{4g} AFM order in Cu doped Mn_3NiN. Density functional theory calculations of the intrinsic contribution to the AHE reveal the nonvanishing Berry curvature in momentum space due to the noncollinear magnetic order. Combined with other attractive properties, the antiperovskite Mn_3AN system offers great potential in AFM spintronics.

DOI: 10.1103/PhysRevB.100.045109

I. INTRODUCTION

Empirically, the anomalous Hall effect (AHE) in conventional ferromagnetic metals is proportional to the net magnetization [1] and was expected to vanish in antiferromagnets. However, it is now well understood that the existence of the AHE is constrained by symmetry and is not necessarily incompatible with AFM order. This principle has been exemplified by the large AHE predicted and realized in various noncollinear AFMs, such as hexagonal Mn_3Sn/Ge and cubic Mn_3Ir/Pt, etc., where the Mn atoms form a kagome lattice along different crystalline planes [2–10]. In these materials, geometric frustration and local symmetries of the magnetic atoms together lead to a chiral noncollinear magnetic order with the essential symmetry breaking for finite AHE, which is also reflected by the small net moment in certain crystalline directions. The large AHE in the hexagonal Mn_3Sn/Ge was argued to be due to Weyl points near the Fermi energy, which can be viewed as monopoles of Berry curvature in momentum space [2–10]. Technologically, the robust AHE at room temperature in these systems makes them attractive for potential applications in spintronics solely based on AFM [11]. Meanwhile, it is interesting to search for similar anomalous Hall antiferromagnets (AHE AFMs) beyond binary Mn compounds, which may have other superior properties.

Antiperovskite manganese nitrides Mn_3AN have received a lot of attention due to a number of unusual physical properties, such as giant negative thermal expansion [12,13], temperature independent resistivity [14], and barocaloric effects [15,16]. All of these phenomena are closely related to the first order phase transition from a high temperature paramagnetic cubic phase into a low temperature noncollinear AFM phase with the so-called Γ_{4g} and Γ_{5g} magnetic structures. It is interesting to notice that the Mn atoms form a 1/4-depleted fcc lattice in these manganese antiperovskites, similar to that in the AHE AFM Mn_3Ir and Mn_3Pt, whose (111) planes are kagome lattices as shown in Figs. 1(a) and 1(b) [17,18]. Therefore, one would expect there to be AHE if the AFM order of the Mn moments is similar to these binary compounds.

In this article, we demonstrate that the AHE could indeed be realized in manganese nitrides, by studying the Mn_3NiN system [13,14,18,19]. We first found that, in stoichiometric Mn_3NiN, a weak signal of AHE is observed below the noncollinear AFM ordering temperature of 180 K, yet disappeared as the temperature further decreases. Using magnetometry and thermal expansion measurements, we then show that, through substantial doping of Cu substituting Ni, the noncollinear AFM order is still preserved in $Mn_3Ni_{1-x}Cu_xN$ polycrystals. Most interestingly, the AHE is enhanced and becomes more robust against temperature after Cu doping. The AHE also does not scale with the net magnetization, contrary to the ferrimagnetic Mn_3CuN system [20,21]. We have also successfully grown single-crystalline $Mn_3Ni_{1-x}Cu_xN$ films, which exhibit large AHE as well. Finally, we analyze the symmetry origin of the AHE in the Γ_{4g} state of Mn_3NiN, complemented by first-principles density functional theory (DFT) calculations revealing the momentum space Berry curvature contributing to the AHE.

II. CRYSTAL STRUCTURE AND X-RAY DIFFRACTION

The successful homogeneous solution of $Mn_3Ni_{1-x}Cu_xN$ powders have been verified by x-ray diffraction in Fig. S1 [22], consistent with previous results [13,14,19]. Figure 1 shows the out of plane x-ray diffraction patterns of Mn_3NiN (c) and $Mn_3Ni_{0.35}Cu_{0.65}N$ (d) 100 nm film on MgO (111) substrate, respectively. The lattice parameter a was estimated to be 3.8699 Å and 3.9012 Å for parent and Cu doped case, slightly smaller than powder case [22,23]. Figure 1(e) shows in-plane x-ray diffraction pattern of $Mn_3Ni_{0.35}Cu_{0.65}N$ film. On the MgO (111) substrate,

*Corresponding author: kan.zhao@physik.uni-augsburg.de

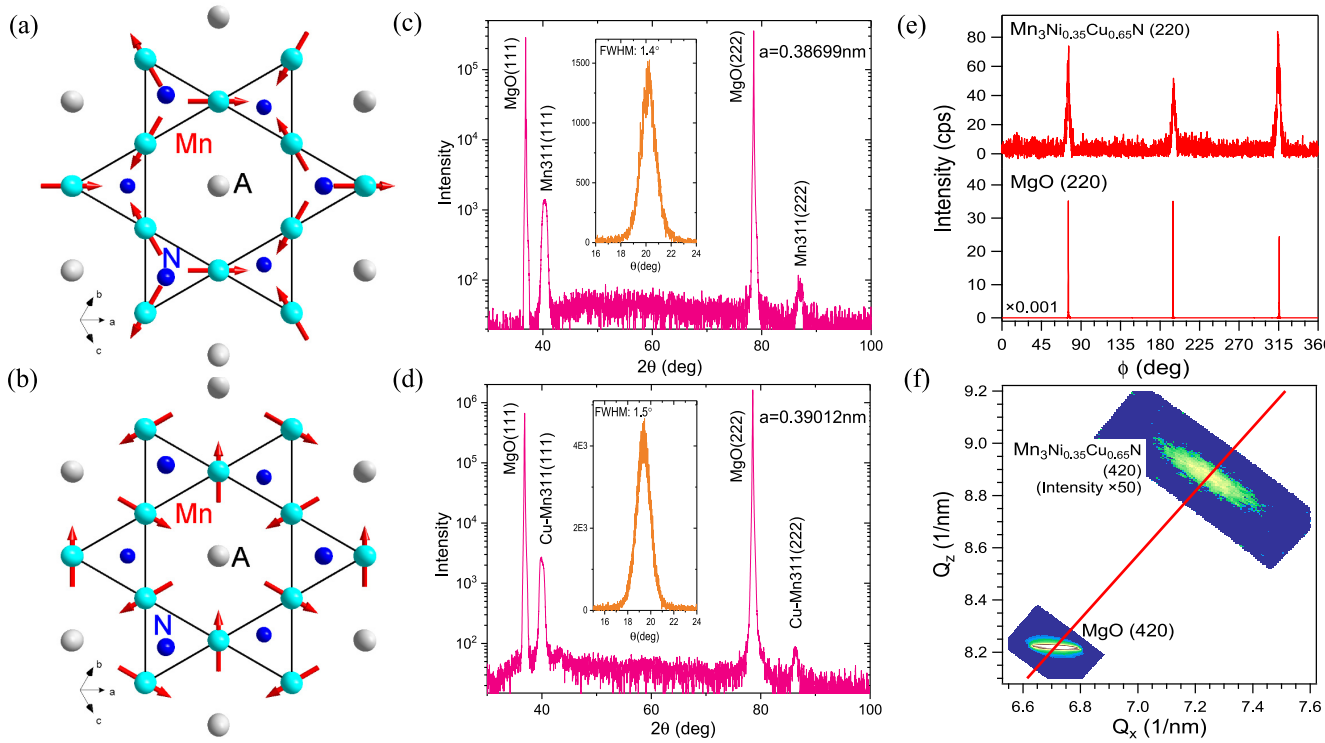

FIG. 1. Magnetic and crystal structures of $Mn_3Ni_{1-x}Cu_xN$. (a)-(b) The Mn kagome lattice with noncollinear AFM structures termed Γ_{4g} and Γ_{5g} in Mn_3AN, respectively. (c)-(d) Out of plane x-ray diffraction pattern for Mn_3NiN 100 nm film and $Mn_3Ni_{0.35}Cu_{0.65}N$ 100 nm film on MgO (111) substrate, with the rocking curves as an inset. (e) In-plane x-ray diffraction data of $Mn_3Ni_{0.35}Cu_{0.65}N$ 100 nm film grown on MgO (111) substrate, with three fold symmetry of (220) peak, (f) Reciprocal space map around (420) reflection, with the solid line as the relaxation line.

(111)-orientated films are epitaxially grown with three fold symmetry of (220) peak. Figure 1(f) displays the reciprocal space map of $Mn_3Ni_{0.35}Cu_{0.65}N$ film on MgO (111) substrate. The (420) peak is observed on the relaxation line, indicating no stain condition of our high quality film.

III. MAGNETIC PROPERTIES AND THERMAL EXPANSION MEASUREMENT

Figure 2(a) shows the temperature dependence of magnetic susceptibilities in field-cooling (FC) procedures under 500 Oe for $Mn_3Ni_{1-x}Cu_xN$ specimens with $x = 0$, 0.3, 0.5, 0.7, 0.8, and 1, respectively. The pure Mn_3NiN shows the AFM transition at 260 K, consistent with previous results [13,14,19], with the magnetic moment only on the Mn site, evidenced by neutron measurement on powders before [18]. The Cu doping continuously decreases the temperature of the AFM transition and increases the low temperature $\chi(T)$, until the system becomes ferrimagnetic which is similar to pure Mn_3CuN, with transition temperature $T_N = 260$ K, 255 K, 230 K, 205K, 190 K, and 160 K, respectively. Besides, the transition temperature is taken as the onset point of the sharp transition for all the samples, except for the $x = 0.3$ case, determined as the middle point of the board transition. Above T_N, the samples are paramagnetic, and the inverse susceptibility $\chi^{-1}(T)$ can be fitted to the Curie-Weiss formula [Fig. 2(b)]. Figure 2(c) summarizes the phase diagram of the $Mn_3Ni_{1-x}Cu_xN$ system, by plotting the T_N versus Cu doping level. Also shown in the plot are the Curie-Weiss temperature and the effective moment obtained from the Curie-Weiss fitting. Similar to the $x = 0$ case, the $x = 0.3$, 0.5, and 0.7 samples exhibit negative Curie-Weiss temperature, suggesting AFM-type interaction, which becomes nearly zero for $x = 0.8$, and about +100 K for the ferrimagnetic Mn_3CuN [20]. When $x > 0.7$, accompanying the change of magnetic ground state, the effective moment μ_{eff} sharply decreases.

As already verified by neutron diffraction experiments in various Mn_3AN systems [18,24–26], the negative thermal expansion there is due to the volume expansion from the paramagnetic cubic phase to the noncollinear AFM phase, while there is no such effect from the paramagnetic-ferrimagnetic transition in Mn_3CuN. As shown in Fig. 2(d), for $Mn_3Ni_{1-x}Cu_xN$ with $x = 0$, 0.5, and 0.7, all three specimens exhibit large volume expansion through a sharp transition at T_N. Moreover, the Cu doped samples show even larger volume expansion than pure Mn_3NiN. The weak anomaly at 120 K in the same plot is due to the AFM transition of MnO impurities [27], supported by the x-ray diffraction data in Fig. S1. The anomaly around 250 K comes from the capacitive dilatometer based measurement system [28]. Together with the magnetic results, our thermal expansion measurements provide clear evidence on the persistence of the noncollinear AFM order in $Mn_3Ni_{1-x}Cu_xN$ for $x < 0.7$.

As predicted and observed in Mn_3Sn and Mn_3Pt [2–4,7,10], a small remnant net magnetization is always accompanying the essential symmetry breaking that leads to AHE. Pure Mn_3NiN exhibits a small hysteresis in the isothermal magnetization $M(H)$ curve at 180 K as shown

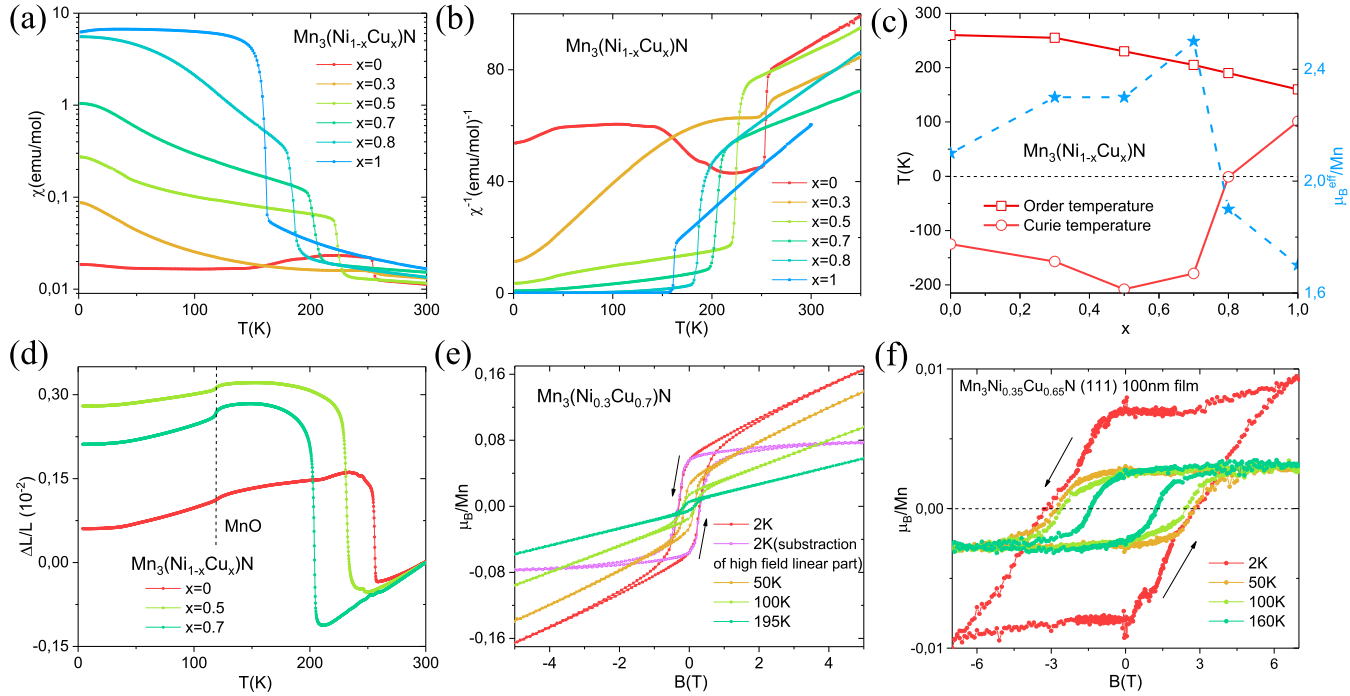

FIG. 2. Magnetic properties and thermal expansion of $Mn_3Ni_{1-x}Cu_xN$. (a)–(b) dc magnetic susceptibility and inverse susceptibility measured in $H = 500$ Oe in $Mn_3Ni_{1-x}Cu_xN$ with several different Cu doping levels x from 2 K to 350 K under field cooling. (c) Phase diagram of $Mn_3Ni_{1-x}Cu_xN$ ($0 < x < 1$), including the experimental AFM transition temperature, the Curie-Weiss temperature, and the effective moment vs Cu doping level. The latter two are obtained from Curie-Weiss fitting of the high-temperature susceptibilities. (d) Temperature-dependent relative length change $[\Delta L/L = [L(T) - L(300\,\mathrm{K})]/L(300\,\mathrm{K})]$ for $Mn_3Ni_{1-x}Cu_xN$ for $x = 0$, 0.5, and 0.7, obtained upon increasing temperature. (e) Isothermal magnetization $M(H)$ for $Mn_3Ni_{0.3}Cu_{0.7}N$ at various temperatures, with saturation moment at 2 K also shown (see text). (f) Out of plane $M(H)$ for $Mn_3Ni_{0.35}Cu_{0.65}N$ 100 nm film on MgO (111) substrate at various temperatures.

in Fig. S2(a) [22]. However, the hysteresis is suppressed as temperature decreases, consistent with a spin glass type behavior observed at 2 K. As shown in Fig. S2 (b) and (c) with $x = 0.3$ and 0.5, the coercive field is still large at 50 K, similar to the pure Mn_3NiN system at 100 K [22]. Doping Cu in Mn_3NiN can gradually stabilize the small ferromagnetic (FM) component and presumably the magnetic structure that hosts AHE. This is best illustrated for the $Mn_3Ni_{0.3}Cu_{0.7}N$ specimen in Fig. 2(e). A small FM component appears below 205 K, and keeps increasing as temperature decreases. After subtracting the H-linear component in the high field region, presumably due to MnO impurities, the saturation moment is about $0.006\mu_B$/Mn at 195 K, $0.05\mu_B$/Mn at 50 K, and $0.08\mu_B$/Mn at 2 K, much smaller than its effective moment, $2.5\mu_B$/Mn from the Curie-Weiss fitting. The coercive field also increases with decreasing temperature and reaches 0.3 T at 2 K.

Figure S3 shows the out of plane isothermal magnetization $M(H)$ curves of $Mn_3Ni_{0.35}Cu_{0.65}N$ (111) 100 nm film after subtracting the large signal from MgO (111) substrate [22]. A rather weak remnant magnetization is clearly observed in Fig. 2(f), with the saturation moment $\sim 0.003\mu_B$/Mn above 50 K and $0.01\mu_B$/Mn at 2 K, due to symmetry-allowed spin canting in the noncollinear state. This weak moment has a similar size to that in Mn_3Sn and Mn_3Pt [4,10], and checks with our DFT calculations below. Its direction is expected to be perpendicular to the kagome plane if the magnetic order is indeed Γ_{4g}. Presumably due to the crystalline order of the (111) films enhancing the magnetocrystalline anisotropy leading to a (111)-directed weak moment, we find the (111) orientated film shows much larger coercive field—1.5 T at 160 K and 2.5 T at 100 K and 50 K—than the polycrystalline $Mn_3Ni_{0.3}Cu_{0.7}N$ in Fig. 2(e).

IV. TRANSPORT PROPERTIES

Next we focus on the transport properties of $Mn_3Ni_{1-x}Cu_xN$ samples, in particular the AHE. Figure 3(a) shows weak signal of the AHE at 180 K in pure Mn_3NiN, consistent with the small FM component shown in Fig. S2. This signal rapidly decreases with temperature, leaving only the normal Hall signal at 2 K, with the carrier density estimated to be 1.4×10^{22} cm^3. Mn_3NiN (111) film exhibits similar behavior as shown in Fig. S4 [22].

Above 205 K, the magnetoresistance (MR) of the $Mn_3Ni_{0.3}Cu_{0.7}N$ specimen increases as H^2 as shown in Fig. 3(b), consistent with normal metal behavior. Below 205 K, clear hysteresis appears with the same coercive field value as in the $M(H)$ curve. The clear positive MR at 2 K and 100 K is also similar to that in Mn_3Sn [8]. The slightly negative MR at 195 K is likely due to strong magnetic fluctuations close to T_N.

Most interestingly, Fig. 3(c) displays large AHE in the AFM state of $Mn_3Ni_{0.3}Cu_{0.7}N$ specimen, with the same

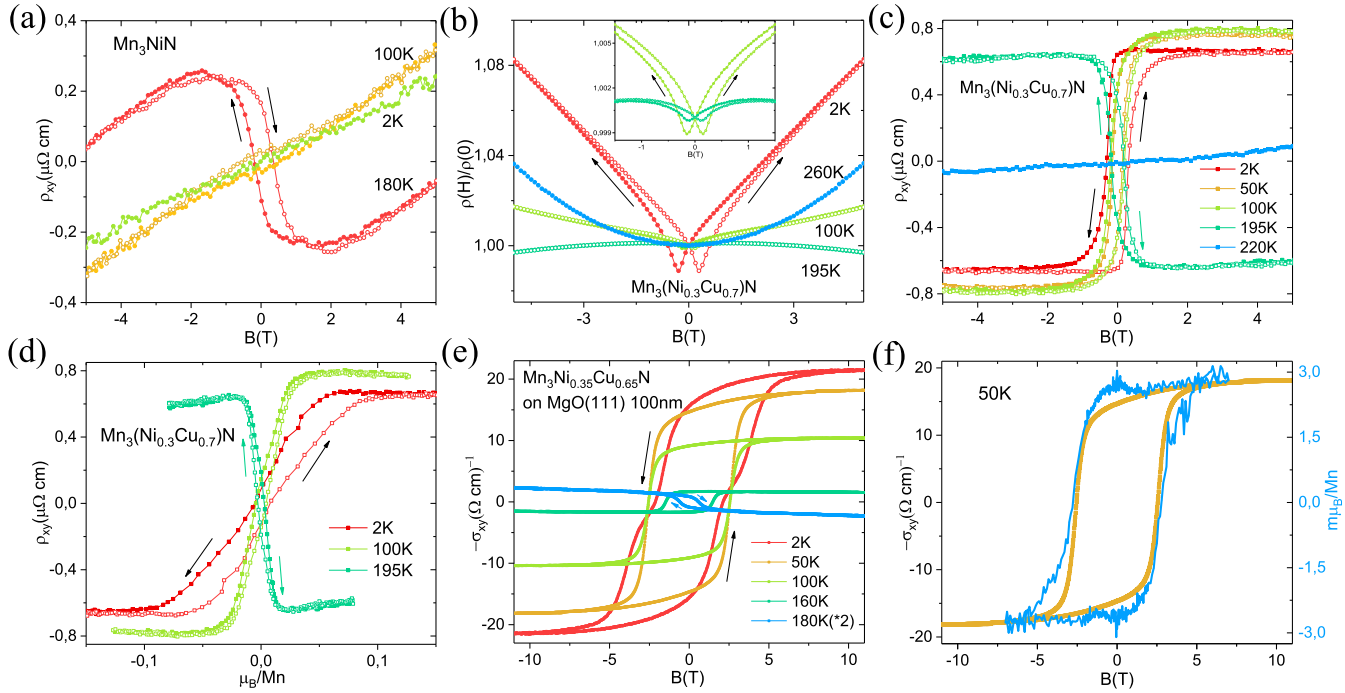

FIG. 3. Transport properties including the AHE in $Mn_3Ni_{1-x}Cu_xN$. (a) Hall resistivity results from a sintered specimen of Mn_3NiN at 180 K, 100 K, and 2 K, respectively. (b) Field dependence of the longitudinal resistivity $\rho(H)/\rho(0)$ of $Mn_3Ni_{0.3}Cu_{0.7}N$ at various temperatures, with the low field region at 195 K and 100 K enlarged in the inset. (c) Field dependence of the Hall resistivity ρ_{xy} of $Mn_3Ni_{0.3}Cu_{0.7}N$ at various temperatures, with the AHE clearly observed below 205 K. (d) Dependence of ρ_{xy} on magnetization of $Mn_3Ni_{0.3}Cu_{0.7}N$ at 195 K, 100 K, and 2 K, respectively. (e) The anomalous Hall conductivity (AHC) versus field measured in single crystalline $Mn_3Ni_{0.35}Cu_{0.65}N$ film on MgO (111) substrate at various temperatures (see text). (f) Comparison of the Hall conductivity and isothermal magnetization of (111) 100 nm film at 50 K.

coercive field as in the $M(H)$ and MR curves. There is also a sign change of the ordinary Hall resistance between 195 K and 100 K, suggesting a transition from hole-type carriers above 195 K to electron-type carriers below 100 K. To further determine the origin of such large AHE, we plot the Hall resistance ρ_{xy} versus the magnetization M in Fig. 3(d). Similar to the arguments used for decomposing different contributions to the AHE in Mn_3Sn [4] and Mn_3Ge [5], the hysteresis with a sharp sign change in $\rho_{xy}(M)$ indicates the AFM origin of the AHE. In contrast, ρ_{xy} of the sintered Mn_3CuN in Fig. S5 [22] is dominated by a contribution proportional to M.

Further, the high quality epitaxial $Mn_3Ni_{0.35}Cu_{0.65}N$ film on MgO (111) substrate enables us to extract the anomalous Hall conductivity (AHC) from the resistivity data, which can be more directly compared with theory. According to the longitudinal and Hall resistance data in Fig. S6 [22], the Hall conductivity σ_{xy} is estimated using $\sigma_{xy} = -\rho_{xy}/\rho_{xx}^2$, which exceeds 20 $(\Omega\,\mathrm{cm})^{-1}$ at 2 K in Fig. 3(e). Similar to the powder case, the switching of AHC is very sharp, except for an additional anomaly at 2 K. Both magnetization and the Hall conductivity of the (111) orientated film exhibit similar coercive field, as shown in Fig. 3(f) at 50 K, indicating the large AHC is directly related with the noncollinear AFM order. The (111) orientated film also shows the sign change of the ordinary Hall signal in Fig. 3(e), which has not been observed in Mn_3Sn and Mn_3Pt [4,10], and deserves future study.

V. DFT CALCULATION AND DISCUSSION

As already mentioned in Sec. I, the Γ_{4g} order of Mn_3NiN is essentially identical to the order of Mn moments in cubic Mn_3Ir and Mn_3Pt, and for the same symmetry reason as in the latter cases it should have the AHE. In contrast, the Γ_{5g} state has a cubic symmetry that forbids AHE. To get a more quantitative estimate of its size in pure Mn_3NiN, which may allow us to make connections with the Cu-doped samples, we performed DFT calculations of the intrinsic AHC of the Γ_{4g} phase of Mn_3NiN [22,29–31]. The band structure and Berry curvature summed over filled bands plotted along high-symmetry lines in the Brillouin zone are shown in Fig. 4. We find that the local spin moment on each Mn is $2.7\mu_B$ with a net moment of $\sim 0.007\mu_B$/Mn, qualitatively agreeing with the experimental results. However, the calculated $\sigma_{\mathrm{AH}} = 525$ $(\Omega\,\mathrm{cm})^{-1}$ [along the (111) direction] is much larger than the experimental value. It is well known that the intrinsic and extrinsic contributions to the AHE are difficult to separate in experiments unless the systems show quantum AHE, in which only the intrinsic contribution survives. Therefore, the intrinsic contribution alone is not usually enough for comparison with experiments. Nonetheless, the large difference between the calculated results and the experimental value is likely to be due to the modification of the electronic structure near Fermi surface by the significant amount of Cu doping. The neutron measurements indicate that, right below 260 K, the Mn_3NiN system is in the Γ_{4g} state [18]. But the Mn moments

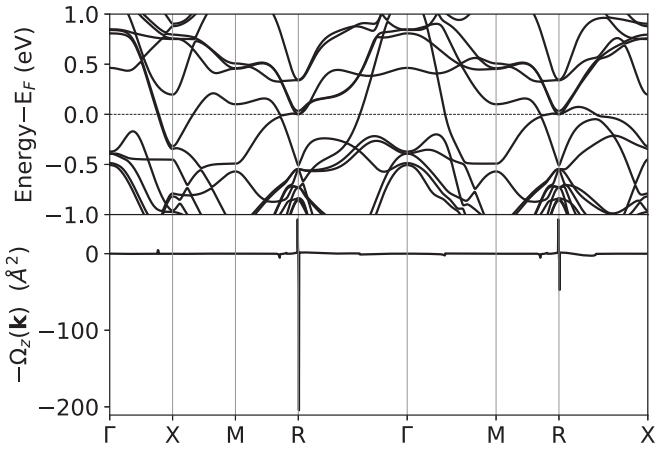

FIG. 4. DFT calculations of Γ_{4g} Mn_3NiN. Band structure (top) and Berry curvature summed over filled bands (bottom) along high-symmetry lines of the Brillouin zone.

rotate toward the Γ_{5g} state with decreasing temperature, which becomes dominant below 100 K [18]. The Cu doping is therefore essential in stabilizing the Γ_{4g} order at low temperatures, which allows AHE. However, its quantitative influence on the AHE in the Γ_{4g} state may depend on many system specific details and will be studied in the future.

VI. CONCLUSION

In conclusion, we have shown that the Cu-doped Mn_3NiN system is a noncollinear antiferromagnet having the AHE that goes beyond binary Mn compounds. The latter encounter potential nonwetting and interfacial oxidation problems during the epitaxial thin-film growth on oxide substrates [10]. Thus it is much easier to obtain a high quality epitaxial $Mn_3Ni_{1-x}Cu_xN$ film on oxide substrates, giving much advantage for the preparation of multilayer devices in the future. Combined with other attractive properties of the antiperovskite nitride systems, our finding may open a new avenue for their application in antiferromagnetic spintronics.

Note added. Recently, we became aware of several papers about the AHE in Mn_3AN system [32–34]. The experimental paper reported the observation of AHE in Mn_3NiN film, stabilized by the strain between film and substrate [34]. Meanwhile, we adopt a totally different strategy, namely Cu substituting on Ni site in $Mn_3Ni_{1-x}Cu_xN$ to stabilize the AHE.

ACKNOWLEDGMENTS

The authors would like to thank German Hammerl, Sven Esser, Maximilian Uhl, and Anton Jesche for helpful discussion and experimental attempt. The work in Augsburg was supported by the German Research Foundation through the priority program SPP 1666. The work in Nagoya was supported by JSPS KAKENHI Grant No. 17K17801 and Kato foundation for Promotion of Science. T.H. also acknowledges Research Grant for Young Scientists (Research Center for Materials Backcasting Technology, School of Engineering, Nagoya University). This work utilized the RMACC Summit supercomputer, which is supported by the National Science Foundation (Awards No. ACI-1532235 and No. ACI-1532236), the University of Colorado Boulder, and Colorado State University. The RMACC Summit supercomputer is a joint effort of the University of Colorado Boulder and Colorado State University.

[1] N. Nagaosa, J. Sinova, S. Onoda, A. H. MacDonald, and N. P. Ong, Rev. Mod. Phys. **82**, 1539 (2010).
[2] H. Chen, Q. Niu, and A. H. MacDonald, Phys. Rev. Lett. **112**, 017205 (2014).
[3] J. Kübler and C. Felser, Europhys. Lett. **108**, 67001 (2014).
[4] S. Nakatsuji, N. Kiyohara, and T. Higo, Nature (London) **527**, 212 (2015).
[5] N. Kiyohara, T. Tomita, and S. Nakatsuji, Phys. Rev. Appl. **5**, 064009 (2016).
[6] A. K. Nayak, J. E. Fischer, Y. Sun, B. Yan, J. Karel, A. C. Komarek, C. Shekhar, N. Kumar, W. Schnelle, J. Kübler *et al.*, Sci. Adv. **2**, e1501870 (2016).
[7] H. Yang, Y. Sun, Y. Zhang, W.-J. Shi, S. S. Parkin, and B. Yan, New J. Phys. **19**, 015008 (2017).
[8] K. Kuroda, T. Tomita, M.-T. Suzuki, C. Bareille, A. Nugroho, P. Goswami, M. Ochi, M. Ikhlas, M. Nakayama, S. Akebi *et al.*, Nat. Mater. **16**, 1090 (2017).
[9] J. Liu and L. Balents, Phys. Rev. Lett. **119**, 087202 (2017).
[10] Z. Liu, H. Chen, J. Wang, J. Liu, K. Wang, Z. Feng, H. Yan, X. Wang, C. Jiang, J. Coey *et al.*, Nat. Electron. **1**, 172 (2018).
[11] L. Šmejkal, Y. Mokrousov, B. Yan, and A. H. MacDonald, Nat. Phys. **14**, 242 (2018).
[12] K. Takenaka and H. Takagi, Appl. Phys. Lett. **87**, 261902 (2005).
[13] K. Takenaka, M. Ichigo, T. Hamada, A. Ozawa, T. Shibayama, T. Inagaki, and K. Asano, Sci. Technol. Adv. Mater. **15**, 015009 (2014).
[14] L. Ding, C. Wang, L. Chu, J. Yan, Y. Na, Q. Huang, and X. Chen, Appl. Phys. Lett. **99**, 251905 (2011).
[15] D. Matsunami, A. Fujita, K. Takenaka, and M. Kano, Nat. Mater. **14**, 73 (2015).
[16] D. Boldrin, E. Mendive-Tapia, J. Zemen, J. B. Staunton, T. Hansen, A. Aznar, J.-L. Tamarit, M. Barrio, P. Lloveras, J. Kim *et al.*, Phys. Rev. X **8**, 041035 (2018).
[17] D. Fruchart and E. F. Bertaut, J. Phys. Soc. Jpn. **44**, 781 (1978).
[18] M. Wu, C. Wang, Y. Sun, L. Chu, J. Yan, D. Chen, Q. Huang, and J. W. Lynn, J. Appl. Phys. **114**, 123902 (2013).
[19] L. Ding, C. Wang, Y. Sun, C. V. Colin, and L. Chu, J. Appl. Phys. **117**, 213915 (2015).
[20] E. Chi, W. Kim, and N. Hur, Solid State Commun. **120**, 307 (2001).
[21] T. Matsumoto, T. Hatano, T. Urata, K. Iida, K. Takenaka, and H. Ikuta, Phys. Rev. B **96**, 205153 (2017).
[22] See Supplemental Material at http://link.aps.org/supplemental/10.1103/PhysRevB.100.045109 for additional details about

polycrystalline sample preparation, single crystalline film growth, and physical property measurements, as well as the methods for first-principles calculations.

[23] H. Tashiro, R. Suzuki, T. Miyawaki, K. Ueda, and H. Asano, J. Korean Phys. Soc. **63**, 299 (2013).

[24] S. Iikubo, K. Kodama, K. Takenaka, H. Takagi, and S. Shamoto, Phys. Rev. B **77**, 020409(R) (2008).

[25] K. Kodama, S. Iikubo, K. Takenaka, M. Takigawa, H. Takagi, and S. Shamoto, Phys. Rev. B **81**, 224419 (2010).

[26] C. Wang, L. Chu, Q. Yao, Y. Sun, M. Wu, L. Ding, J. Yan, Y. Na, W. Tang, G. Li *et al.*, Phys. Rev. B **85**, 220103(R) (2012).

[27] W. Roth, Phys. Rev. **110**, 1333 (1958).

[28] R. Küchler, T. Bauer, M. Brando, and F. Steglich, Rev. Sci. Instrum. **83**, 095102 (2012).

[29] P. Giannozzi, S. Baroni, N. Bonini, M. Calandra, R. Car, C. Cavazzoni, D. Ceresoli, G. L. Chiarotti, M. Cococcioni, I. Dabo *et al.*, J. Phys.: Condens. Matter **21**, 395502 (2009).

[30] A. A. Mostofi, J. R. Yates, Y.-S. Lee, I. Souza, D. Vanderbilt, and N. Marzari, Comput. Phys. Commun. **178**, 685 (2008).

[31] D. R. Hamann, Phys. Rev. B **88**, 085117 (2013).

[32] X. Zhou, J.-P. Hanke, W. Feng, F. Li, G.-Y. Guo, Y. Yao, S. Blügel, and Y. Mokrousov, Phys. Rev. B **99**, 104428 (2019).

[33] G. Gurung, D.-F. Shao, T. R. Paudel, and E. Y. Tsymbal, Phys. Rev. Materials **3**, 044409 (2019).

[34] D. Boldrin, I. Samathrakis, J. Zemen, A. Mihai, B. Zou, B. Esser, D. McComb, P. Petrov, H. Zhang, and L. F. Cohen, arXiv:1902.04357.

Correction: The name of a funding agency listed in the Acknowledgments was set incorrectly during the tagging process and has now been fixed.